Molecular & Cellular Biomechanics

Tech Science Press

DOI: 10.32604/mcb.2022.018958

ARTICLE

Nuclear Stress-Strain State over Micropillars: A Mechanical *In silico* Study

Rachele Allena[1,*] **and Denis Aubry**[2]

[1]LJAD, UMR CNRS 7351, Université Côte d'Azur, Nice, 06300, France

[2]Université Paris-Saclay, CentraleSupélec, UMR CNRS 8579, Laboratoire de Mécanique des Sols, Structures et Matériaux, Gif-sur-Yvette, 91190, France

[*]Corresponding Author: Rachele Allena. Email: rachele.allena@unice.fr

Received: 26 August 2021 Accepted: 20 October 2021

ABSTRACT

Cells adapt to their environment and stimuli of different origin. During confined migration through sub-cellular and sub-nuclear pores, they can undergo large strains and the nucleus, the most voluminous and the stiffest organelle, plays a critical role. Recently, patterned microfluidic devices have been employed to analyze the cell mechanical behavior and the nucleus self-deformations. In this paper, we present an *in silico* model to simulate the interactions between the cell and the underneath microstructured substrate under the effect of the sole gravity. The model lays on mechanical features only and it has the potential to assess the contribution of the nuclear mechanics on the cell global behavior. The cell is constituted by the membrane, the cytosol, the lamina, and the nucleoplasm. Each organelle is described through a constitutive law defined by specific mechanical parameters, and it is composed of a fluid and a solid phase leading to a viscoelastic behavior. Our main objective is to evaluate the influence of such mechanical components on the nucleus behavior. We have quantified the stress and strain distributions in the nucleus, which could be responsible of specific phenomena such as the lamina rupture or the expression of stretch-sensitive proteins.

KEYWORDS

Nuclear mechanics; micropillared substrate; *in silico* model

1 Introduction

Cells continuously adapt themselves to their environment and stimuli they received (i.e., chemical, electrical, mechanical, …) [1–3]. More specifically, they are able to undergo large strains during confined migration through sub-cellular or sub-nuclear pores. During such a process, the nucleus, the most voluminous and the stiffest cellular organelle, plays a critical role [4,5]. Some cells such as cancerous cells can even undergo the rupture of the nuclear lamina to be able to migrate across healthy tissues [6,7]. Therefore, quantifying nucleus strains and stresses can be crucial to diagnose cancer and other pathologies in patients.

To do so, patterned microfluidic devices have been employed during the last few years in order to characterize the cell mechanical behaviour [8,9] and the nucleus self-deformations [10–13] and shape changes [14,15] induced by mechanical forces, which are due to the interaction between the cell and the topological surface. Assays on micropillared substrates involve successive steps: (i) contact between the

cell and the pillars, (ii) adhesion of the cell on the pillars surface, (iii) cell spreading, (iv) cell polarization and (v) cell crawling.

A series of analytical and numerical models exist in the literature focusing on the interactions between the cell and a flat substrate. The former provides information on the spreading process with no excessive computational cost [16–19]. The latter, which may be discrete [20–22] or continuum [15,23–25], allows to investigate the intra-cellular rearrangement or to obtain quantitative results at the global or the local scale. In our previous paper [26], we have proposed an *in silico* two-dimensional (2D) model which simulates the first three steps (i.e., contact, adhesion and spreading) of the interaction between the cell and the micropillared substrate and provides insights on the mechanisms inducing nuclear deformation. We have been able to determine the role of the gravity and of the actin fibers above and beneath the nucleus responsible for a pushing and a pulling force, respectively.

In the present paper, we have adapted the model presented in [26] and we have focused on step one only (i.e., contact between the cell and the pillars). The cell and nucleus behaviours are described using specific mechanical tools (i.e., constitutive laws, mechanical properties, fluid and solid phase balance). By performing a sensibility study, our objective has been to determine the influence of these parameters on the interaction between the cell and underneath micropillared substrate. Then, the model provides the nucleus stress and strain fields over time and gives insights on the global cellular behavior that can be further explored experimentally.

In Section 2, we describe the mathematical framework of the model including the geometry (Section 2.1), the constitutive laws governing the behaviour of the cell and of its components (Section 2.2), the external forces applied to the cell (Sections 2.3 and 2.4) and the numerical implementation (Section 2.5). The results of the different simulations are presented in Section 3 and some conclusions and perspectives are drawn in Section 4.

2 Material and Methods

2.1 Cell Geometry

Given the symmetry conditions, we consider here the cell Ω_c in its initial configuration as a semicircle of radius r_c (Fig. 1). It is constituted by the membrane Ω_m (external radius $r_m = r_c$ and thickness t_m), the cytosol Ω_{cs} (external radius r_{cs}), the lamina Ω_l (external radius r_l and thickness t_l) and the nucleoplasm Ω_{np} (external radius r_{np}) (Fig. 1). The membrane and the cytosol form the cytoplasm Ω_{cp}, whereas the lamina and the nucleoplasm form the nucleus Ω_n. Each component of the cell Ω_i is described *via* a spatial characteristic function g_i, which is the composition of a regularized Heaviside function H (equal to 0 and 1 for negative and positive argument, respectively), and a level set function l_i. Then, the characteristic functions describing the cell and its components are the following:

$$g_c = H \circ l_c = H \circ \left(\|\mathbf{p} - \mathbf{c}_{c,p}^2\| - r_c^2 \right) \tag{1}$$

$$g_{np} = H \circ l_{np} = H \circ \left(\|\mathbf{p} - \mathbf{c}_{\mathrm{c,p}}^{\mathbf{2}}\| - \mathrm{r}_{\mathrm{np}}^2 \right) \tag{2}$$

$$g_l = H \circ l_l - g_{np} = H \circ \left(\|\mathbf{p} - \mathbf{c}_{c,p}^2\| - r_l^2 \right) - g_{np} \tag{3}$$

$$g_{cs} = H \circ l_{cs} - g_l - g_{np} = H \circ \left(\|\mathbf{p} - \mathbf{c}_{c,p}^2\| - r_{cs}^2 \right) - g_l - g_{np} \tag{4}$$

$$g_m = H \circ l_m - g_l - g_{np} - g_{cs} = H \circ \left(\|\mathbf{p} - \mathbf{c}_{c,p}^2\| - r_m^2 \right) - g_l - g_{np} - g_{cs} \tag{5}$$

with $\|\cdot\|$ the euclidean norm of a vector, $\boldsymbol{p}$ the initial position of any point of the system and $\mathbf{c}_{c,p}$ the center of the cell of coordinates (c_x, c_y).

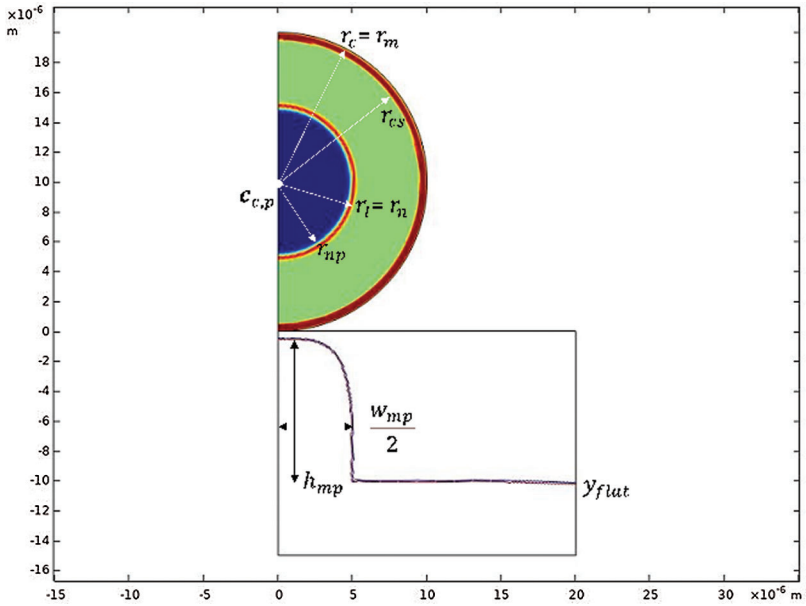

Figure 1: Cell and substrate geometry at t = 0 s. The cell has an external radius r_c and it is constituted by the nucleus (nucleoplasm in blue and lamina in orange), external radius $r_n = r_l$, and the cytoplasm (cytosol in green and membrane in red), external radius r_m. The substrate is constituted by a micropillar of height h_{mp} and width w_{mp} and a flat region placed at y-coordinate y_{flat}

2.2 Constitutive Laws

Each cell component is composed of a solid and a fluid phase. To simplify the approach, we assume that both phases deform in parallel like in a Kelvin–Voigt model. Consequently, the overall stress $\boldsymbol{S}$ and the deformation $\boldsymbol{F}$ can be expressed as

$$\mathbf{S} = c_s \mathbf{S}_{s,i} + c_f \mathbf{S}_f \tag{6}$$

$$\mathbf{F} = \mathbf{F}_s = \mathbf{F}_f \tag{7}$$

where the subscripts s and f indicate the solid and the fluid phases, respectively, while the subscript i indicates a specific constitutive law for the solid phase, as described in the followings (Section 2.2.1), and c_s and c_f the respective concentrations are given by

$$c_s = c_{s,m} g_m + c_{s,cs} g_{cs} + c_{s,l} g_l + c_{s,np} g_{np} \tag{8}$$

$$c_f = c_{f,m} g_m + c_{f,cs} g_{cs} + c_{f,l} g_l + c_{f,np} g_{np} \tag{9}$$

$$c_{s,m} = 1 - c_{f,m} \tag{10}$$

$$c_{s,cs} = 1 - c_{f,cs} \tag{11}$$

$$c_{s,l} = 1 - c_{f,l} \tag{12}$$

$$c_{s,np} = 1 - c_{f,np} \tag{13}$$

2.2.1 The Solid Phase

When describing the solid phase of an isotropic elastic material, for stability reasons, its strain energy must be poly-convex with respect to the three invariants I_1, I_2 and I_3 [27,28], which are expressed as follows:

$$I_1 = Tr(\mathbf{C}) \tag{14}$$

$$I_2 = det(\mathbf{C})Tr\left(\mathbf{C}^{-1}\right) \tag{15}$$

$$I_3 = det(\mathbf{C}) \tag{16}$$

where $\mathbf{C} = \mathbf{F}^T\mathbf{F}$ is the dilatation tensor.

From a physical point of view, I_1 describes the length variations of the system in the three directions, I_2 gives both the shear and length deformations and I_3 describes the volume variations of the system [29,30]. Then, given the multistructural organization of the cell, it is important that all the invariants are considered. Nonetheless, in the present model, four different materials have been tested to point out their specific features. Specifically, we have implemented:

1. A standard Saint-Venant material, which only depends on the first and second invariants I_1 and I_2 [31,32] and it is able to capture the deformations along the lines (i.e., the fibers deformations);
2. A Neo-Hookean compressible material, which depends on the first I_1 and third I_3 invariants [33,34] and allows to take into account the deformations along the lines and inside the volumes (i.e., both fibers and cytosol plus nucleoplasm deformations);
3. The Mooney-Rivlin and Yeoh compressible materials which depend on the three invariants [25,35] and describe the deformations along lines, volumes and surfaces (i.e., the membrane and the lamina). Furthermore, the Yeoh material takes into account the successive softening and stiffening behavior of an elastic material made of fibers.

The second Piola Kirchhoff stress $\mathbf{S}_{s,i}$, where the subscript i indicates the material, is expressed as follows:

– for the standard Saint-Venant material $\mathbf{S}_{s,SV}$ reads

$$\mathbf{S}_{s,SV} = \lambda_s Tr(\mathbf{E})\mathbf{I} + 2\mu_s\mathbf{E} \tag{17}$$

with $\lambda_s = \dfrac{E_i\upsilon_c(1+\upsilon_c)}{(1-2\upsilon_c)(1+\upsilon_c)}$ and $\mu_s = \dfrac{E_i}{2(1+\upsilon_c)}$ (E_i and υ_c are the Young moduli of each cell component and the Poisson ratio, respectively), *Tr* the trace of a tensor, ***E*** the Green Lagrange tensor and ***I*** the identity matrix;

– for the compressible neo-Hookean material $\mathbf{S}_{s,NH}$ is given by

$$\mathbf{S}_{s,NH} = \mu_s\left(\mathbf{I} - \mathbf{C}^{-1}\right) + \lambda_s ln(J)\mathbf{C}^{-1} \tag{18}$$

with $J = det\ \mathbf{F}$;

– for the Mooney-Rivlin material $\mathbf{S}_{s,MR}$ can be written as

$$\mathbf{S}_{s,MR} = 2[\alpha_{MR} + \beta_{MR}(Tr\mathbf{C})]\mathbf{I} - 2\beta_{MR}\mathbf{C} + \left[\lambda_{MR} ln(J) - 2\alpha_{MR}J^{2/3} - 4\beta_{MR}J^{4/3}\right]\mathbf{C}^{-1} \tag{19}$$

with $\alpha_{MR} = \dfrac{\mu_s}{2} - \beta_{MR}$, $\beta_{MR} = \dfrac{\mu_s}{0.4}$ and $\lambda_{MR} = \lambda_s + \dfrac{2}{3}\mu_s$ [26];

– finally, for the Yeoh material $\mathbf{S}_{s,Y}$ reads

$$\begin{aligned}\mathbf{S}_{s,Y} &= 2\Big[\alpha_{MR} + \beta_{MR}(Tr\mathbf{C}) + \alpha_{Y1}(Tr\mathbf{C}) + \alpha_{Y2}(Tr\mathbf{C})^2\Big]\mathbf{I} - 2\beta_{MR}\mathbf{C} \\ &+ \Big[\lambda_{MR} ln(J) - 2\alpha_{MR}J^{2/3} - 4\beta_{MR}J^{4/3}\Big]\mathbf{C}^{-1}\end{aligned} \tag{20}$$

where $\alpha_{Y1} = -0.5\alpha_{MR}$ and $\alpha_{Y2} = 0.1\alpha_{MR}$ are two constants [26].

2.2.2 The Fluid Phase

For the fluid phase of the cell, a Newtonian viscous fluid is considered but it must be defined in the Lagrangian configuration in order to ensure the compatibility with the solid phase. Thus, the Cauchy stress $\boldsymbol{\sigma}_f$ is classically given by

$$\boldsymbol{\sigma}_\mathbf{f} = \lambda_f Tr\big(\mathbf{D}_f\big)\mathbf{I} + 2\mu_f \mathbf{D}_f \tag{21}$$

where λ_f and μ_f are the isotropic and deviatoric viscosities, respectively and $\mathbf{D}_f$ must be expressed as a function of the rate of the dilatation tensor $\mathbf{C}_f$ as follows:

$$\mathbf{D}_f = \mathbf{F}_f^{-T}\frac{d\mathbf{C}_f}{dt}\mathbf{F}_f^{-1} \tag{22}$$

with the superscript T indicating the transpose of a matrix.

Since $\mathbf{C}_f = \mathbf{C}$ and $\mathbf{F}_f = \mathbf{F}$ (Eq. (7)), substituting $\boldsymbol{\sigma}_\mathbf{f}$ in Eq. (21), we obtain the expression of the second Piola-Kirchhoff

$$\mathbf{S}_f = \frac{J\lambda_f}{2}Tr\left(\mathbf{C}^{-1}\frac{d\mathbf{C}}{dt}\right)\mathbf{C}^{-1} - J\mu_f\frac{d\mathbf{C}^{-1}}{dt} \tag{23}$$

2.3 The Gravity Force

The cell is submitted to the gravity force $\mathbf{f}_g$

$$\mathbf{f}_g = -\rho_c t_g g\mathbf{i}_y \tag{24}$$

where ρ_c is the initial cell density, g the gravitational acceleration and $\mathbf{i}_y$ the vertical unit vector. t_g is employed here to smoothly apply the gravity force to ensure the computation fast convergence. It is the composition of a regularized Heaviside function H and a level set function l_g and it reads

$$t_g = H \circ l_g = H \circ \big(-t + T_g\big) \tag{25}$$

with t the time and T_g a constant.

2.4 The Cell Environment

As the gravity is applied, the cell settles down and starts interacting with the underneath micropillared substrate, which is constituted by a micropillar and a flat region and it is defined by a characteristic function g_s as follows:

$$g_s = g_{mp} + g_{flat} = H \circ \big(l_{mp} + l_{flat}\big) = H \circ \left[-\left(\frac{\mathbf{x} - x_{mp}}{w_{mp}}\right)^4 - \left(\frac{y - y_{mp}}{h_{mp}}\right)^4 + 1\right] + H \circ \big[-\mathbf{y} + y_{flat}\big] \tag{26}$$

where l_{mp} and l_{flat} are two level set functions, $\boldsymbol{x}$ and $\boldsymbol{y}$ are the actual coordinates of any point in the system, x_{mp} and y_{mp} define the position of the micropillars, w_{mp} and h_{mp} define the width and the height of the micropillar, respectively and y_{flat} is the position of the flat region with respect to the y-axis.

Once the cell approaches the substrate, the contact force $\mathbf{f}_{ct}$ applies over a very thin layer corresponding to the intersection between the cell and the substrate. We have shown that $\mathbf{f}_{ct}$ can be approximated by a volume force [26] and it can be computed *via* a penalization technique as follows:

$$\mathbf{f}_{ct} = \mu_{ct} g_{flat} \mathbf{cof}(\mathbf{F}) \mathbf{n}_{flat} + \mu_{ct} g_{mp} \mathbf{cof}(\mathbf{F}) \mathbf{n}_{mp} \tag{27}$$

where μ_{ct} is the penalization coefficient. $\mathbf{cof}(\mathbf{F})$ is the cofactor matrix defined as $J_c \mathbf{F}^{-\mathrm{T}}$ and it is employed here to bring back to the initial configuration the outward normal vectors to the micropillar ($\mathbf{n}_{mp}$) and to the flat substrate ($\mathbf{n}_{flat}$), which are obtained as follows:

$$\mathbf{n}_{mp} = \frac{\nabla_x l_{mp}}{\|\nabla_x l_{mp}\|} \tag{28}$$

$$\mathbf{n}_{flat} = \frac{\nabla_x l_{flat}}{\|\nabla_x l_{flat}\|} \tag{29}$$

2.5 Finite Element Model

The global equilibrium of the system in the initial configuration can be expressed as

$$Divp(\boldsymbol{FS}) + \boldsymbol{f_g} = \rho_c \boldsymbol{a} \tag{30}$$

with *Div* the first order divergence operator in the initial configuration, and $\boldsymbol{a}$ the acceleration.

In order to employ a classical finite element approach, we multiply each term of Eq. (30) by the kinematically admissible displacement test function $\boldsymbol{w}$ and we integrate over the cellular domain Ω_c. Then, by using some algebraic operations and by applying the Stokes theorem, we obtain

$$-\int_{\Omega_c} Tr\left[\mathbf{FS}\left(\mathbf{D_p w}\right)^T\right] dV_{\mathbf{p}} + \int_{\partial\Omega_c} (\mathbf{w}, \mathbf{FS}(\mathbf{n_c})) dS_{\mathbf{p}} + \int_{\Omega_c} \left(\rho_p \mathbf{g} - \rho_p \mathbf{a}, \mathbf{w}\right) dV_{\mathbf{p}} = 0 \tag{31}$$

where $n_{\mathbf{c}}$ is the outward normal to the cell and the first and the third term indicate the internal cellular stress and the volume forces, respectively. The second term describes the surface forces applied to the cell and specifically the contact force f_{ct} between the cell and underneath micropillared substrate. As mentioned above (Section 2.4), $\mathbf{f}_{ct}$ is applied through a very thin layer. Thus, the surface integral in Eq. (31) can be written as a volume integral over the penalization thickness h_p. Therefore, Eq. (31) becomes

$$-\int_{\Omega_c} Tr\left[\mathbf{FS}\left(\mathbf{D_p w}\right)^T\right] dV_{\mathbf{p}} + \int_{\Omega_c} \left(\rho_c \mathbf{g} + h_p \mathbf{f}_{ct} - \rho_c \mathbf{a}, \mathbf{w}\right) dV_{\mathbf{p}} = 0 \tag{32}$$

Eq. (26) has been manually implemented using the weak form tool in COMSOL Multiphysics. The spatial discretization is obtained via quadratic polynomials for each isoparametric element of the mesh (mesh size between 0.3 μm and 1 μm). The time discretization is achieved via a second-order backward differentiation formula (BDF). The solution is computed using a nonlinear Newton scheme with a relative tolerance of 1% on the displacement error estimation.

3 Results and Discussion

The radii of the cell (r_c) and the nucleus (r_n) have been set equal to 10 μm and 5 μm, respectively. The membrane and the lamina have a thickness t_m and t_l of 0.5 μm and 0.1 μm [36], respectively (Fig. 1). The cell density ρ_c and the Poisson ratio υ_c have been set to 1000 kg/m^3 and 0.45, respectively. The isotropic (λ_f) and deviatoric (μ_f) viscosities are equal to 1000 Pa·s and 5×10^{-3} Pa·s, respectively. The Young's moduli have been set to $E_m = 100$ Pa [31], $E_{cs} = 10$ Pa [37], $E_l = 1000$ Pa [31,38] and $E_{np} = 10$ Pa [39]. The gravity force is gently applied on the cell and reaches its maximum at $2T_g = 10000\ s$. Through the gravity, the cell comes in

contact with the micropillar which has a width (w_{mp}) and a height (h_{mp}) of 20 μm and 9.5 μm, respectively (Fig. 1). All the simulations last for T_{end} = 18000 s. All the parameters of the model are listed in Table 1. For each series of simulations that we are going to present, the nucleus stress has been evaluated in terms of Mises Cauchy stress σ_{Mises}, whereas the strains have been quantified through three variables: (i) $J_1 = I_1 = Tr(\mathbf{C})$ to detect the fibers elongation, (ii) $J_2 = Tr(\mathbf{C}^2)$ to evaluate the shear and length deformations and (iii) $J_3 = I_3 = det(\mathbf{C})$ to assess the surface variations.

Table 1: Main geometrical and mechanical parameters of the model

Variable	Definition	Value	Units	Reference
r_c	Cell radius	10	μm	
r_m	Membrane radius	10	μm	
t_m	Membrane thickness	0.5	μm	
r_{cs}	Cytosol radius	9.5	μm	
r_n	Nucleus radius	5	μm	
r_l	Lamina radius	5	μm	
t_l	Lamina thickness	0.1	μm	[36]
r_{cs}	Nucleoplasm radius	4.9	μm	
$c_{f,m}$	Fluid coefficient for the membrane	0.5		
$c_{f,cs}$	Fluid coefficient for the cytosol	0.5		
$c_{f,l}$	Fluid coefficient for the lamina	0.5		
$c_{f,np}$	Fluid coefficient for the nucleoplasm	0.5		
ρ_c	Cell's density	1000	Kg/m^3	[36]
υ_c	Cell's Poisson ratio	0.45		
E_m	Membrane Young's modulus	100	Pa	[31]
E_{cs}	Cytosol Young's modulus	10	Pa	[37]
E_l	Lamina Young's modulus	1000	Pa	[31,38]
E_{np}	Nucleoplasm Young's modulus	10	Pa	[39]
λ_f	Isotropic viscosity	1000	Pa·s	
μ_f	Deviatoric viscosity	5×10^{-3}	Pa·s	
g	Gravitational acceleration	9.81	m/s^2	
T_g	Time constant	5000	s	
y_{flat}	Substrate vertical position	−10	μm	
x_{mp}	Micropillar x position	0	μm	
y_{mp}	Micropillar y position	−10	μm	
w_{mp}	Micropillar width	10	μm	
h_{mp}	Micropillar height	9.5	μm	
μ_{ct}	Penalization coefficient	5×10^7	Pa·s	
T_{end}	End of the simulation	18000	s	

3.1 Cell Components Constitutive Law

For the first series of simulations, we have tested different constitutive laws for the cell components. All the parameters defining each constitutive law are reported in Table 1. The fluid coefficients have been set equal to $c_{f,m} = c_{f,cs} = c_{f,l} = c_{f,np} = 0.5$.

The Saint-Venant material model is the simplest and mostly used in the literature, but it is not robust enough to describe very large deformations. The Neo-Hookean and the Mooney-Rivlin materials are efficient in considering large strains, but they do not exhibit typical stiffness-softening followed by hardening during deformation. Finally, the Yeoh model is theoretically the most consistent, but it is much more complex than the others due to a higher number of parameters to define (Eq. (21)).

The evolution as a function of time of the Mises stress σ_{Mises} and J_1, J_2 and J_3 in the nucleus Ω_n are shown in Fig. 2. The highest value of the von Mises stress (1.042 Pa) is obtained for the Mooney-Rivlin material (Fig. 2a). The Neo-Hookean and the Yeoh materials are very close with a maximum of 1.032 Pa and 1.027 Pa, respectively. For the Saint-Venant material, the maximum is slightly lower (0.86 Pa).

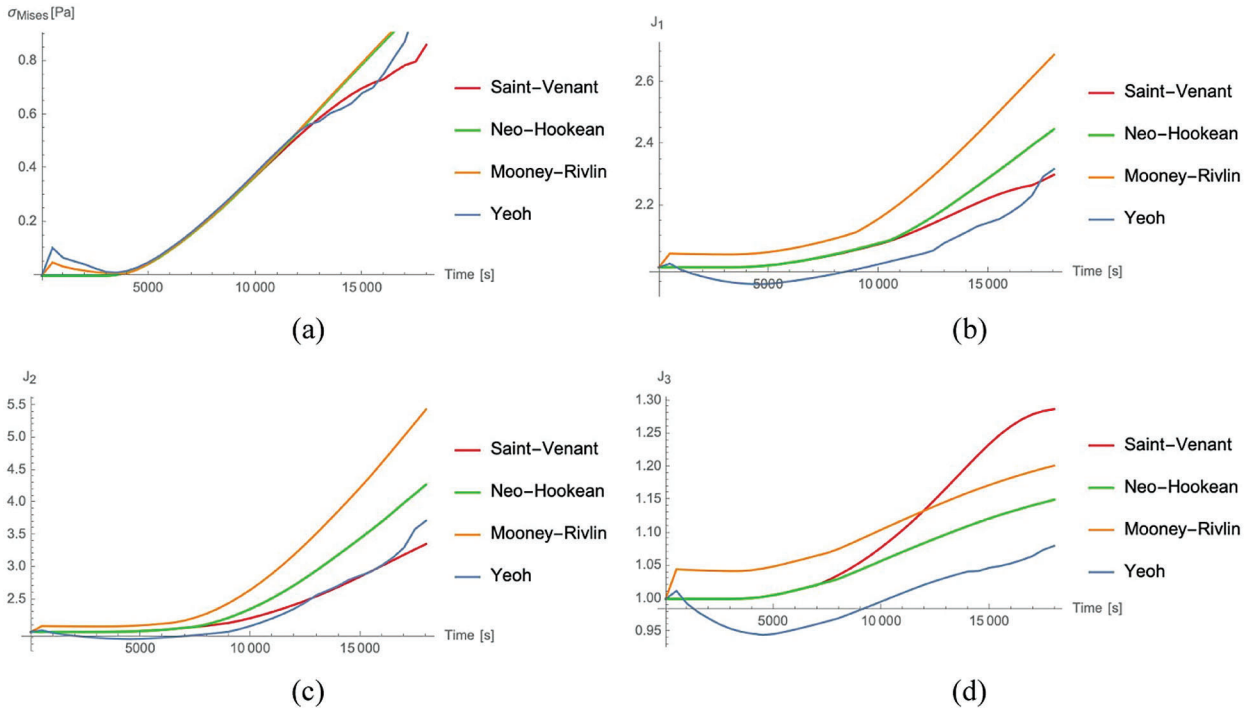

Figure 2: von Mises Cauchy stress σ_{Mises} (a) and J_1 (b), J_2 (c) and J_3 (d) in the nucleus Ω_n as a function of time for different materials: Saint-Venant (red line), Neo-Hookean (green line), Mooney-Rivlin (orange line) and Yeoh (blue line)

For the strains, the Mooney Rivlin material provides the maximum values of J_1 and J_2 (2.68 and 5.44, respectively) and $J_3 = 1.20$ (orange line in Figs. 2b, 2c and 2d). For the Saint-Venant material, $J_1 = 2.30$, $J_2 = 3.35$ and $J_3 = 1.28$ (red line in Figs. 2b, 2c and 2d). The Yeoh material shows low values for all the three strains indicators, more specifically $J_1 = 2.31$, $J_2 = 3.72$ and $J_3 = 1.08$ (blue line in Figs. 2b, 2c and 2d). The Neo-Hookean material provide $J_1 = 2.44$, $J_2 = 4.27$ and $J_3 = 1.15$ (green line in Figs. 2b, 2c and 2d).

We can estimate the contribution of the nucleus to the total cell deformation. In terms of fibers elongation (J_1), we found that when implementing the Mooney Rivlin material the nucleus undergoes 56% of the global deformation, whereas with the Saint-Venant material only 49%. Regarding the shear and length variations

(J_2), the Mooney Rivlin ensures again the highest nucleus contribution (81%) *vs.* the Yeoh material for which the nucleus supplies for only 61%. Finally, for the surface variations (J_3), contributions between 18% (Saint-Venant material) and 23% (Mooney Rivlin material) are found. In Fig. 3 we show the overall deformation of the cell and the nucleus at t = 18000 s for the different material models.

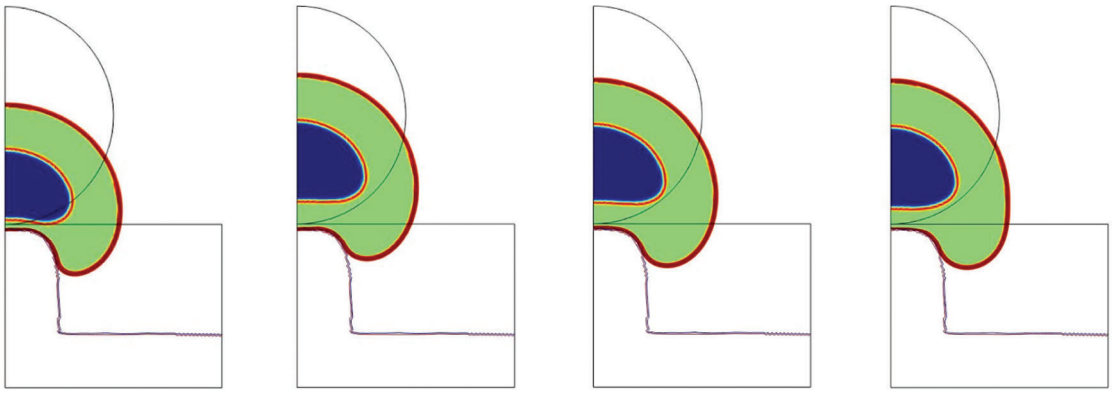

Figure 3: Total cell deformation at t = 18000 s for the Saint-Venant (a), the Neo-Hookean (b), the Mooney-Rivlin (c) and the Yeoh (d) material (blue = nucleoplasm, orange = lamina, green = cytosol, red = membrane)

Since the cell is composed by several organelles having different structures and geometries, there is a need for a constitutive macroscopic law able to describe the stresses associated to such heterogeneous strains. More specifically, taking into account these stresses implies low values of J_1, J_2 and J_3. Thus, according to our results, the Yeoh material model seems to be the most appropriate, which confirms the theoretical remarks at the beginning of the section.

3.2 Nucleus Fluid and Solid Phases

For the second series of simulations we have evaluated the influence of the fluid-solid phases of the lamina and of the nucleoplasm on the nucleus behaviour. Specifically, we have let vary $c_{f,l}$ and $c_{f,np}$ from 0.1 to 0.9, testing all the combinations for a total of 24 simulations (one combination has not converged, i.e., $c_{f,l} = c_{f,np} = 0.9$). The values of $c_{f,m}$ and $c_{f,cs}$ have been set to 0.5. The Young moduli of the cell organelles are those defined at the beginning of Section 3.

In Fig. 4, values of σ_{Mises} (Fig. 4a) and of J_1, J_2 and J_3 (Figs. 4b, 4c and 4d) in the nucleus Ω_n are presented. σ_{Mises} is maximal for $c_{f,l} = 0.1$ and $c_{f,np} = 0.7$ and it is equal to 1.32 Pa.

On the one side, the maximal strains are found for $c_{f,l} = 0.7$ and $c_{f,np} = 0.9$ and they are equal to $J_1 = 4.08$ (71% of the total cell deformation), $J_2 = 15.20$ (163% of the total cell deformation) and $J_3 = 1.31$ (20% of the total cell deformation). This combination corresponds to $\sigma_{Mises} = 0.45$ Pa. In Fig. 5a, the total deformation of the cell organelles at t = 18000 s is shown and one can notice that the nucleus is particularly stretched. Such a large strain could exacerbate the sensor functions of the nucleus as it has been observed in previous experimental studies [40–42] and therefore induce cell motility *via* the activation of specific stretch-sensitive proteins.

On the other side, the lowest values of J_1 and J_2 (4.08 and 15.20, respectively) are found for $c_{f,l} = 0.3$ and $c_{f,np} = 0.1$, with $\sigma_{Mises} = 1.08$ Pa, and they correspond to 51% and 58% of the total cell deformation. Whereas the minimal value of J_3 (1.31) has been obtained for $c_{f,l} = 0.9$ and $c_{f,np} = 0.1$, with $\sigma_{Mises} = 0.85$ Pa, and it corresponds to 23% of the total cell deformation.

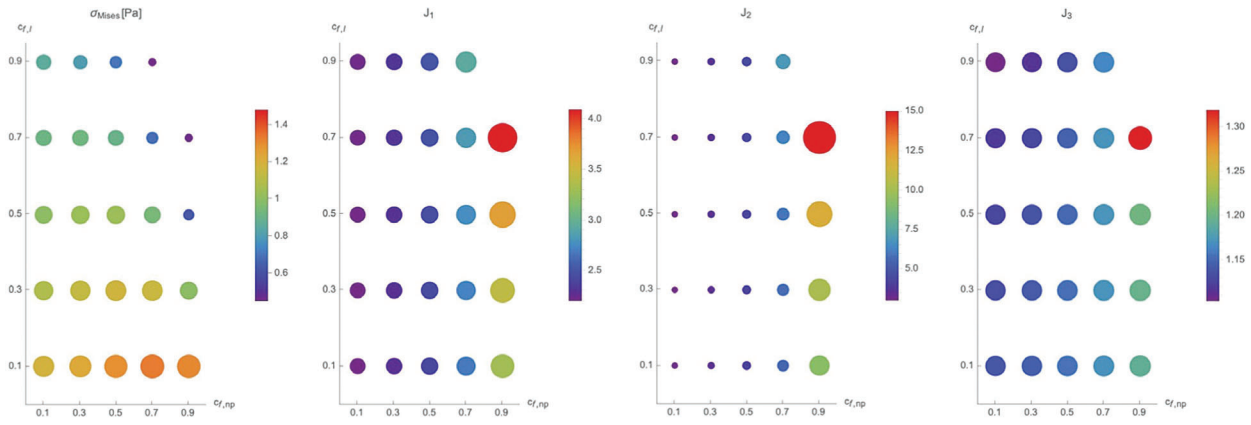

Figure 4: Maximal value of σ_{Mises} (a) and J_1 (b), J_2 (c) and J_3 (d) in the nucleus Ω_n at t = 18000 s as a function of E_l and E_{np}

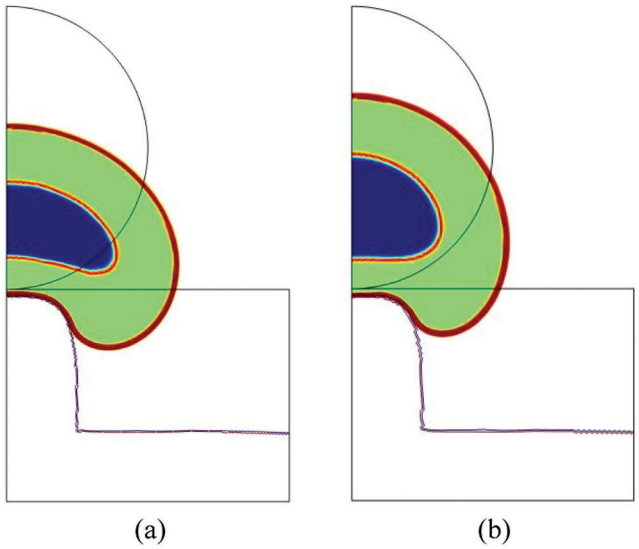

Figure 5: Total cell deformation at t = 18000 s for $c_{f,np} = 0.9$ and $c_{f,l} = 0.7$ (a) and for $E_l = 1000$ Pa and $E_{np} = 10$ Pa (b) (blue = nucleoplasm, orange = lamina, green = cytosol, red = membrane)

3.3 Nucleus Mechanical Properties

For the last series of simulations, we have let vary the Young's moduli of the nucleoplasm (E_{np}) and of the lamina (E_l). Specifically, we have set E_{np} = 10, 30, 50, 70, 90 Pa and E_l = 1000, 1500, 2000, 2500, 3000 Pa for a total of 25 simulations, which have all converged. For the fluid and solid phases of the organelles, we have set here $c_{f,np} = c_{f,l} = c_{f,cs} = c_{f,m} = 0.5$.

Fig. 6, we show the results in terms of Mises Cauchy stress σ_{Mises} (Fig. 6a) and of J_1, J_2 and J_3 (Figs. 6b, 6c and 6d) in the nucleus Ω_n. σ_{Mises} is maximal for E_{np} = 10 Pa and E_l = 2000 Pa and it is equal to 1.47 Pa. The maximal values of J_1 and J_2 are observed for E_{np} = 10 Pa and E_l = 1000 Pa (σ_{Mises} = 1.03 Pa) and they are equal to 2.44 (53% of the total cell deformation) and 4.27 (69% of the total cell deformation), respectively) (Fig. 5b). For J_3, the maximal value is equal to 1.16 (22% of the total cell deformation) and

it is found for E_{np} = 10 Pa and E_l = 3000 Pa, with σ_{Mises} = 1.47 Pa. As for the minimal values of J_1 and J_2, they are equal to 2.11 (50% of the total cell deformation) and 2.26 (51% of the total cell deformation), respectively. They are found for E_{np} = 90 Pa and E_l = 1500 Pa and provide σ_{Mises} = 0.55 Pa. The lowest J_3 has been found equal to 1.10 (24% of the total cell deformation) for E_{np} = 90 Pa and E_l = 1000 Pa with σ_{Mises} = 0.46 Pa.

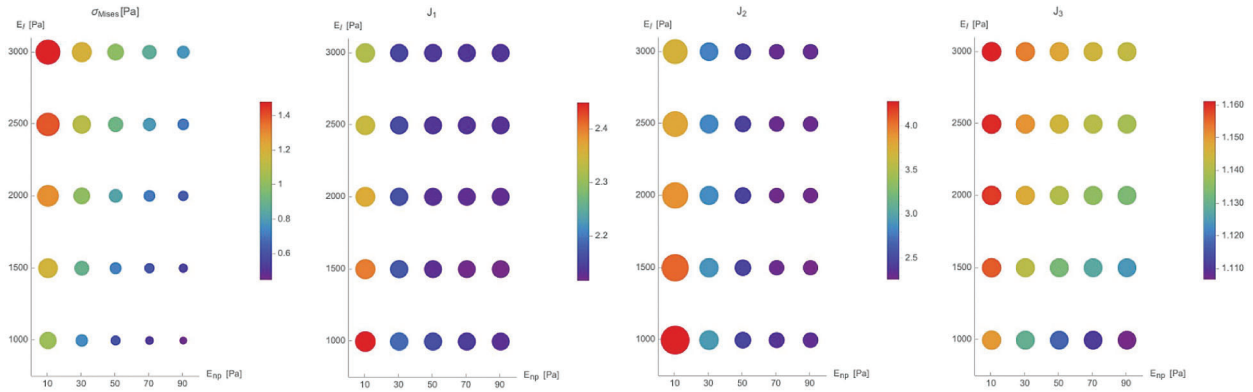

Figure 6: Maximal value of σ_{Mises} (a) and J_1 (b), J_2 (c) and J_3 (d) in the nucleus Ω_n at t = 18000 s as a function of $c_{f,np}$ and $c_{f,l}$

3.4 Comparison with Experimental Data

In the previous series of simulations, t_{end} has been set equal to 18000 s. In this section we propose to go further (t_{end} = 24000 s) in order to explore more severe nucleus deformations and to be able to compare our numerical results with experimental observations.

We have run three additional simulations (S_1, S_2, S_3) for which a Saint-Venant material model has been implemented. However, the mechanical properties of the nucleus (i.e., E_{np} and E_l) as well as the nucleus fluid concentration (i.e., $c_{f,np}$ and $c_{f,l}$) have been modified as reported in Table 2.

Table 2: Main parameters of simulations S_1, S_2, S_3

Simulation	Parameter			
	E_{np} [Pa]	E_l [Pa]	$c_{f,np}$	$c_{f,l}$
S_1	10	1000	0.5	0.5
S_2	10	1000	0.9	0.7
S_3	10	10	0.9	0.7

From a quantitative point of view, the results in terms of maximal stress (σ_{Mises}) and strain (J_1, J_2, J_3) in the nucleus Ω_n are reported in Table 3.

In Fig. 7, the total cell and nucleus deformation at t = 24000 s is shown. One can notice that for S_1 (Fig. 7a), the final shape of the nucleus is not significantly different from the previous simulations. However, as the fluid concentration of the nucleoplasm and the lamina is increased (S_2), the nucleus undergoes a higher deformation (Fig. 7b) leading to an important reduction of the distance between the nuclear lamina and the micropillar boundary. Additionally, the nucleus starts acquiring a 'peanut' shape

as it has been experimentally observed for different cellular phenotypes including mesenchymal stem cells, osteosarcoma cells and bone marrow stroma cells [11–14]. Such an outcome becomes even more evident when the nuclear lamina is ablated (S_3) (Fig. 7c), which correspond to a decrease of the lamina Young's modulus in the numerical simulation. This confirms specific experimental observations according to which tumor cells are able to soften their nucleus and adjust their mechanical properties in order to facilitate extravasation [43].

Table 3: Maximal values of σ_{Mises}, J_1, J_2 and J_3 in the nucleus Ω_n at t = 24000 s for S_1, S_2, S_3.

	Variable			
Simulation	σ_{Mises} [Pa]	J_1	J_2	J_3
S_1	2.55	2.36	4.96	1.27
S_2	0.58	2.89	6.64	1.11
S_3	1.13	3.05	6.92	0.86

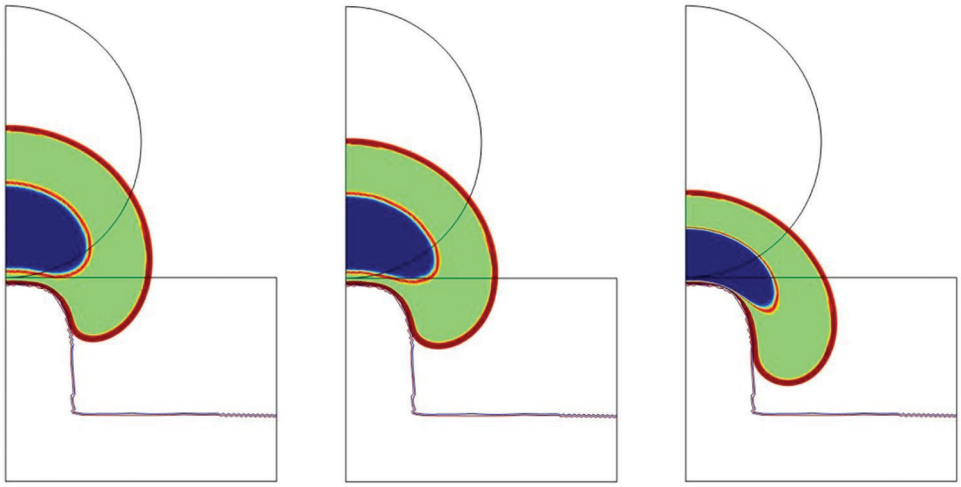

Figure 7: Total cell deformation at t = 24000 s for S_1 (a), S_2 (b) and S_3 (c) (blue = nucleoplasm, orange = lamina, green = cytosol, red = membrane)

In [12–14] a shape index (*SI*) parameter is used to quantify the nucleus self-deformation. SI is defined as follows:

$$SI = 4\pi \frac{S}{l^2} \tag{33}$$

where S and l are the nucleus surface and perimeter, respectively. *SI* is equal to 1 for a perfect circle (i.e., no deformation), whereas it is equal to 0 for a straight line. In [12–14], *SI* is measured in the plan perpendicular to the micropillars. This is not possible in our model since we are in 2D. Nonetheless, we believe that it is even more interesting to measure *SI* in the sagittal plan to quantify the nucleus self-deformation, but also its penetration. We found that *SI* is equal to 0.32, 0.26 and 0.21 for S_1, S_2 and S_3, respectively indicating a significant nucleus deformation in particular when the nuclear lamina is ablated (i.e., S_3).

4 Conclusions

In this paper we have presented a 2D computational model to investigate the interactions between the cell and the micropillared substrate. The cell is initially suspended and gently meets the pillar due to the gravity force. Then, the contact force between the cell and the pillar is applied over a very thin layer.

The model is equipped with specific mechanical tools, namely the constitutive laws describing the cell components, their mechanical properties, and the fluid and solid phase mixture for each component. Our main objective has been establishing a correlation between such elements and the nucleus stress-strain state. To do so, a thorough sensibility study has been performed. More specifically, three series of simulations have been run: (i) the first one involves different materials models to describe the cell behaviour, i.e., Saint-Venant, Neo-Hookean, Mooney-Rivlin and Yeoh materials, (ii) the second one focuses on the balance between the fluid and solid phases of the lamina and nucleoplasm, (iii) the third one takes into account the variation of the mechanical parameters (i.e., the Young modulus) of the lamina and the nucleoplasm.

Through the large spectrum of combinations that we have provided, biologists may identify the one corresponding to specific cellular phenotypes or behaviors. Additionally, our model could inspire further experimental investigations to explore the interactions between the cell and the micropillared substrate.

We have been able to quantify the stress and the strain in the nucleus Ω_n. For the former, the Mises Cauchy stress σ_{Mises} has been assessed. For the latter, we have computed J_1, J_2 and J_3 which provide the fibers elongation, the shear and length variations and the surface variations, respectively.

We have shown that the variation of the balance between the fluid and solid phase of the nucleus induces the maximum strains of the nucleus. In fact, we have found that varying $c_{f,l}$ and $c_{f,np}$ provides the highest values of J_1, J_2 and J_3. More specifically, J_1 and J_2 are equal to 4.08 and 15.20 for $c_{f,l} = 0.7$ and $c_{f,np} = 0.9$ and such values are much higher than those found for different constitutive laws (2.68 and 5.244 for the Mooney Rivlin material) and for different values of E_{np} and E_l (2.44 and 4.27 for E_{np} = 10 Pa and E_l = 1000 Pa). For J_3, the maximal values are closer although the highest value (1.31) is still found for the sensibility study on the fluid and solid phases balancing. This outcome confirms the importance of the phases balance and the need to correctly take them into account in the mechanical description of the nucleus. Furthermore, the amount of strain found could have an impact on the nucleus response and more particularly on the expression of strecth-sensitive proteins which could be responsible of cell motility in confined environments [40–42].

In terms of stress, even though the maximal values of the Mises Cauchy stress σ_{Mises} are very close for the three series of simulations, the highest one (1.47 Pa) is found when varying the Young moduli of the lamina and the nucleoplasm. More specifically, such a value is obtained when E_{np} = 10 Pa and E_l = 2000 Pa. This configuration could potentially induce the lamina rupture due to its high stiffness compared to the nucleoplasm. Such a phenomenon can change the lamina structure and therefore have critical consequences in disease like cancer or in genome stability [44–46].

Through some additional simulations, we have been able to compare our numerical results to the experimental observations on different cellular phenotypes. More specifically, we have shown that by increasing the simulation time, the nucleus undergoes significant self deformation and it acquires a ‘peanut’ shape by embracing the micropillar as it has been reported in [11–14]. Such a phenomenon is exacerbated when the nuclear lamina is ablated (i.e., reducing the Young modulus) and it confirms data according to which tumor cells are able to adjust their mechanical properties in order to invade healthy tissues [43].

To conclude, our model, which has been built only using mechanical tools, has drawn a large spectrum of scenarios to analyze and quantify the nucleus stress-strain state. It can help identifying the mechanical

features responsible for specific nucleus responses and their impact on the global cell behavior. Although the interesting results, the present model could be improved in the different ways. First, a three-dimensional description of the system would allow to better evaluate the interactions between the cell and its surroundings and the nucleus role. Secondly, it could be interesting to quantify the pressure gradient in the cell in order to assess the proteins traffic flow to and from the nucleus. Finally, a precise description of the structure of the nuclear lamina could provide new information regarding its rupture and remodelling.

Funding Statement: The authors received no specific funding for this study.

Conflicts of Interest: The authors declare that they have no conflicts of interest to report regarding the present study.

References

1. Mammoto, T., Ingber, D. E. (2010). Mechanical control of tissue and organ development. *Development (Cambridge, England), 137(9),* 1407–1420. DOI 10.1242/dev.024166.
2. Versaevel, M., Grevesse, T., Gabriele, S. (2012). Spatial coordination between cell and nuclear shape within micropatterned endothelial cells. *Nature Communications, 3(1),* 671. DOI 10.1038/ncomms1668.
3. Swift, J., Ivanovska, I. L., Buxboim, A., Harada, T., Dingal, P. C. D. P. et al. (2013). Nuclear Lamin–A scales with tissue stiffness and enhances matrix-directed differentiation. *Science, 341(6149),* 1240104. DOI 10.1126/science.1240104.
4. Friedl, P., Wolf, K., Lammerding, J. (2011). Nuclear mechanics during cell migration. *Current Opinion in Cell Biology, 23(1),* 55–64. DOI 10.1016/j.ceb.2010.10.015.
5. Wolf, K., Te Lindert, M., Krause, M., Alexander, S., Te Riet, J. et al. (2013). Physical limits of cell migration: Control by ECM space and nuclear deformation and tuning by proteolysis and traction force. *The Journal of Cell Biology, 201(7),* 1069–1084. DOI 10.1083/jcb.201210152.
6. Denais, C. M., Gilbert, R. M., Isermann, P., McGregor, A. L., Te Lindert, M. et al. (2016). Nuclear envelope rupture and repair during cancer cell migration. *Science (New York, N.Y.), 352(6283),* 353–358. DOI 10.1126/science.aad7297.
7. Bell, E. S., Lammerding, J. (2016). Causes and consequences of nuclear envelope alterations in tumour progression. *European Journal of Cell Biology, 95(11),* 449–464. DOI 10.1016/j.ejcb.2016.06.007.
8. Lu, H., Koo, L. Y., Wang, W. M., Lauffenburger, D. A., Griffith, L. G. et al. (2004). Microfluidic shear devices for quantitative analysis of cell adhesion. *Analytical Chemistry, 76(18),* 5257–5264. DOI 10.1021/ac049837t.
9. Rosenbluth, M. J., Lam, W. A., Fletcher, D. A. (2008). Analyzing cell mechanics in hematologic diseases with microfluidic biophysical flow cytometry. *Lab on a Chip, 8(7),* 1062–1070. DOI 10.1039/b802931h.
10. Davidson, P. M., Fromigué, O., Marie, P. J., Hasirci, V., Reiter, G. et al. (2010). Topographically induced self-deformation of the nuclei of cells: Dependence on cell type and proposed mechanisms. *Journal of Materials Science. Materials in Medicine, 21(3),* 939–946. DOI 10.1007/s10856-009-3950-7.
11. Badique, F., Stamov, D. R., Davidson, P. M., Veuillet, M., Reiter, G. et al. (2013). Directing nuclear deformation on micropillared surfaces by substrate geometry and cytoskeleton organization. *Biomaterials, 34(12),* 2991–3001. DOI 10.1016/j.biomaterials.2013.01.018.
12. Liu, X., Liu, R., Gu, Y., Ding, J. (2017). Nonmonotonic self-deformation of cell nuclei on topological surfaces with micropillar array. *ACS Applied Materials & Interfaces, 9(22),* 18521–18530. DOI 10.1021/acsami.7b04027.
13. Liu, R., Yao, X., Liu, X., Ding, J. (2019). Proliferation of cells with severe nuclear deformation on a micropillar array. *Langmuir, 35(1),* 284–299. DOI 10.1021/acs.langmuir.8b03452.
14. Pan, Z., Yan, C., Peng, R., Zhao, Y., He, Y. et al. (2012). Control of cell nucleus shapes via micropillar patterns. *Biomaterials, 33(6),* 1730–1735. DOI 10.1016/j.biomaterials.2011.11.023.
15. Hanson, L., Zhao, W., Lou, H. Y., Lin, Z. C., Lee, S. W. et al. (2015). Vertical nanopillars for in situ probing of nuclear mechanics in adherent cells. *Nature Nanotechnology, 10(6),* 554–562. DOI 10.1038/nnano.2015.88.

16. Cuvelier, D., Théry, M., Chu, Y. S., Dufour, S., Thiéry, J. P. et al. (2007). The universal dynamics of cell spreading. *Current Biology, 17(8),* 694–699. DOI 10.1016/j.cub.2007.02.058.
17. Sarvestani, A. S., Jabbari, E. (2008). Modeling the kinetics of cell membrane spreading on substrates with ligand density gradient. *Journal of Biomechanics, 41(4),* 921–925. DOI 10.1016/j.jbiomech.2007.11.004.
18. Nisenholz, N., Rajendran, K., Dang, Q., Chen, H., Kemkemer, R. et al. (2014). Active mechanics and dynamics of cell spreading on elastic substrates. *Soft Matter, 10(37),* 7234–7246. DOI 10.1039/C4SM00780H.
19. Cao, X., Lin, Y., Driscoll, T. P., Franco-Barraza, J., Cukierman, E. et al. (2015). A chemomechanical model of matrix and nuclear rigidity regulation of focal adhesion size. *Biophysical Journal, 109(9),* 1807–1817. DOI 10.1016/j.bpj.2015.08.048.
20. Ingber, D. E. (2003). Tensegrity I. Cell structure and hierarchical systems biology. *Journal of Cell Science, 116(7),* 1157–1173. DOI 10.1242/jcs.00359.
21. Milan, J.-L., Lavenus, S., Pilet, P., Louarn, G., Wendling, S. et al. (2013). Computational model combined with in vitro experiments to analyse mechanotransduction during mesenchymal stem cell adhesion. *European Cells & Materials, 25,* 97–113. DOI 10.22203/eCM.v025a07.
22. Fang, Y., Lai, K. W. C. (2016). Modeling the mechanics of cells in the cell-spreading process driven by traction forces. *Physical Review E, 93(4),* 042404. DOI 10.1103/PhysRevE.93.042404.
23. Etienne, J., Duperray, A. (2011). Initial dynamics of cell spreading are governed by dissipation in the actin cortex. *Biophysical Journal, 101(3),* 611–621. DOI 10.1016/j.bpj.2011.06.030.
24. Golestaneh, A. F., Nadler, B. (2016). Modeling of cell adhesion and deformation mediated by receptor-ligand interactions. *Biomechanics and Modeling in Mechanobiology, 15(2),* 371–387. DOI 10.1007/s10237-015-0694-9.
25. Zeng, X., Li, S. (2011). Multiscale modeling and simulation of soft adhesion and contact of stem cells. *Journal of the Mechanical Behavior of Biomedical Materials, 4(2),* 180–189. DOI 10.1016/j.jmbbm.2010.06.002.
26. Mondésert-Deveraux, S., Aubry, D., Allena, R. (2019). *In silico* approach to quantify nucleus self-deformation on micropillared substrates. *Biomechanics and Modeling in Mechanobiology, 18(5),* 1281–1295. DOI 10.1007/s10237-019-01144-2.
27. Itskov, M., Aksel, N. (2004). A class of orthotropic and transversely isotropic hyperelastic constitutive models based on a polyconvex strain energy function. *International Journal of Solids and Structures, 41(14),* 3833–3848. DOI 10.1016/j.ijsolstr.2004.02.027.
28. Bonet, J., Gil, A. J., Ortigosa, R. (2015). A computational framework for polyconvex large strain elasticity. *Computer Methods in Applied Mechanics and Engineering, 283,* 1061–1094. DOI 10.1016/j.cma.2014.10.002.
29. Holzapfel, G. A. (2000). *Nonlinear solid mechanics: A continuum approach for engineering*. (*1st ed*.) Hoboken: Wiley.
30. Bonet, J., Wood, R. D. (2008). *Nonlinear continuum mechanics for finite element analysis*. (*2nd ed.*) Cambridge: Cambridge University Press.
31. Allena, R., Aubry, D. (2012). Run-and-tumble or look-and-run? A mechanical model to explore the behavior of a migrating amoeboid cell. *Journal of Theoretical Biology, 306,* 15–31. DOI 10.1016/j.jtbi.2012.03.041.
32. Fan, H., Li, S. (2015). Modeling universal dynamics of cell spreading on elastic substrates. *Biomechanics and Modeling in Mechanobiology, 14(6),* 1265–1280. DOI 10.1007/s10237-015-0673-1.
33. Jean, R. P., Chen, C. S., Spector, A. A. (2003). Analysis of the deformation of the nucleus as a result of alterations of the cell adhesion area. *ASME 2003 International Mechanical Engineering Congress and Exposition,* pp. 121–122. Washington, DC, USA.
34. Mokbel, M., Mokbel, D., Mietke, A., Träber, N., Girardo, S. et al. (2017). Numerical simulation of real-time deformability cytometry to extract cell mechanical properties. *ACS Biomaterials Science & Engineering, 3(11),* 2962–2973. DOI 10.1021/acsbiomaterials.6b00558.
35. Wang, H., Biao, Y., Chunlai, Y., Wen, L. (2017). Simulation of AFM indentation of soft biomaterials with hyperelasticity. *IEEE 12th International Conference on Nano/Micro Engineered and Molecular Systems,* pp. 550–553. Los Angeles, CA, USA.

36. Righolt, C. H., Raz, V., Vermolen, B. J., Dirks, R. W., Tanke, H. J. et al. (2011). Molecular image analysis: Quantitative description and classification of the nuclear lamina in human mesenchymal stem cells. *International Journal of Molecular Imaging, 2011(8),* 1–11. DOI 10.1155/2011/723283.
37. Crick, F. H. C., Hughes, A. F. W. (1950). The physical properties of cytoplasm. *Experimental Cell Research, 1(1),* 37–80. DOI 10.1016/0014-4827(50)90048-6.
38. Caille, N., Thoumine, O., Tardy, Y., Meister, J. J. (2002). Contribution of the nucleus to the mechanical properties of endothelial cells. *Journal of Biomechanics, 35(2),* 177–187. DOI 10.1016/S0021-9290(01)00201-9.
39. Vaziri, A., Lee, H., Mofrad, M. R. K. (2006). Deformation of the cell nucleus under indentation: Mechanics and mechanisms. *Journal of Materials Research, 21(8),* 2126–2135. DOI 10.1557/jmr.2006.0262.
40. Lomakin, A. J., Cattin, C. J., Cuvelier, D., Alraies, Z., Molina, M. et al. (2020). The nucleus acts as a ruler tailoring cell responses to spatial constraints. *Science, 370(6514),* eaba2894. DOI 10.1126/science.aba2894.
41. Enyedi, B., Jelcic, M., Niethammer, P. (2016). The cell nucleus serves as a mechanotransducer of tissue damage-induced inflammation. *Cell, 165(5),* 1160–1170. DOI 10.1016/j.cell.2016.04.016.
42. Venturini, V., Pezzano, F., Castro, F. C., Häkkinen, H. M., Jiménez-Delgado, S. et al. (2020). The nucleus measures shape changes for cellular proprioception to control dynamic cell behavior. *Science, 370(6514),* eaba2644. DOI 10.1126/science.aba2644.
43. Roberts, A. B., Zhang, J., Raj Singh, V., Nikolić, M., Moeendarbary, E. et al. (2021). Tumor cell nuclei soften during transendothelial migration. *Journal of Biomechanics, 121(5),* 110400. DOI 10.1016/j.jbiomech.2021.110400.
44. Hatch, E. M. (2018). Nuclear envelope rupture: Little holes, big openings. *Current Opinion in Cell Biology, 52,* 66–72. DOI 10.1016/j.ceb.2018.02.001.
45. Vargas, J. D., Hatch, E. M., Anderson, D. J., Hetzer, M. W. (2012). Transient nuclear envelope rupturing during interphase in human cancer cells. *Nucleus, 3(1),* 88–100. DOI 10.4161/nucl.18954.
46. de Vos, W. H., Houben, F., Kamps, M., Malhas, A., Verheyen, F. et al. (2011). Repetitive disruptions of the nuclear envelope invoke temporary loss of cellular compartmentalization in laminopathies. *Human Molecular Genetics, 20(21),* 4175–4186. DOI 10.1093/hmg/ddr344.